Design and performance of a dual polarizing detector system for broadband astronomical spectroscopy at submillimeter wavelengths

D. A. Naylor[a] and B. G. Gom
Department of Physics, University of Lethbridge, Lethbridge, Alberta T1K 3M4, Canada

P. A. R. Ade
Department of Physics, Queen Mary and Westfield College, London E1 4NS, United Kingdom

J. E. Davis
Cochise Instruments, Hereford, Arizona 85615

The design and performance of a dual polarizing bolometer detector system for use with a polarizing Fourier transform spectrometer to conduct broadband astronomical spectroscopy at submillimeter wavelengths is presented. The system features a fully differential electronics design which virtually eliminates common mode noise. The optical design efficiently rejects unwanted radiation, both spectrally and spatially, while minimizing the effects of resonant optical cavities. The system is cooled by an efficient, closed cycle ^{4}He–^{3}He refrigerator which is cycled under computer control. The noise performance of the system is determined from analysis of electrical, optical, and spectral measurements, and the results are compared with a theoretical bolometer model. © *1999 American Institute of Physics.* [S0034-6748(99)01210-1]

I. INTRODUCTION

In recent years there has been rapid growth in submillimeter astronomy, primarily as a result of technological advances, which has led to the development of sophisticated detector systems and spectrometers.

There are two principal spectroscopic techniques used at submillimeter wavelengths: coherent detection using a heterodyne receiver and incoherent (bolometric) detection using a Fourier transform spectrometer (FTS).[1] While the spectral resolution of a FTS cannot match that of a heterodyne receiver, the broad spectral coverage and intermediate resolution are ideally suited to studies of planetary atmospheres and bright extragalactic objects which have linewidths greater than the bandwidth of heterodyne receivers.[2–4]

Following the development of a polarizing FTS[5] to conduct broadband, intermediate resolution, astronomical spectroscopic observations from the James Clerk Maxwell Telescope (JCMT)[6] using the JCMT facility bolometric detector, UKT14,[7] it became readily apparent that the photometric sensitivity of UKT14 was not being realized in spectroscopic observations. The specific problems encountered were electrical pickup at the detector, extreme microphonic sensitivity of the Dewar, and the presence of several resonant optical cavities within the Dewar which produced an undulating background in the resulting spectrum. Furthermore, since UKT14 contains a single bolometer element, only one half of the radiation processed by the polarizing FTS was detected.

In this article we describe the design and performance of a dual polarizing bolometer detector system which has been developed for use with the polarizing FTS at the JGMT and which operates over the wavelength range of 1100–300 μm.

Careful attention has been given to the optical design to minimize electrical interference and microphonic sensitivity and to reduce the effects of optical interference fringes. The cryogenic system employs closed cycle ^{4}He and ^{3}He pumps, thereby eliminating the need for external vacuum pumps. The electronics feature a novel differential design which virtually eliminates common mode electrical noise from the often hostile telescope environment.

II. DETECTOR SYSTEM

The basic design criteria for the detector system were set by the JCMT and the FTS. The large focal ratio, F, of the JCMT, combined with the long wavelength, defines a large focal plane aperture $(2.44\lambda F)$ which creates difficulties for the design of a cryogenic system with a long hold time. It is therefore essential to reject unwanted radiation efficiently. The design must eliminate or minimize the electrical interference and microphonic sensitivity encountered with UKT14. From a cryogenic standpoint the system must be simple to operate and to recycle.

Based on these criteria, a closed cycle, dual stage ^{4}He–^{3}He refrigerator was selected for the cold stage.[8] This unit was mounted in an Infrared Laboratories[9] extended HD8 Dewar. A schematic diagram of the detector system is shown in Fig. 1.

A. Optical design

The key components of the detector optics and cold stage are shown in Fig. 2. Radiation enters the Dewar through a 76 mm diam, 1 mm thick, polypropylene window, which is strong enough to withstand atmospheric pressure and yet has a transmittance that exceeds 95% over the wavelength range of interest. Under pressure the window bows in,
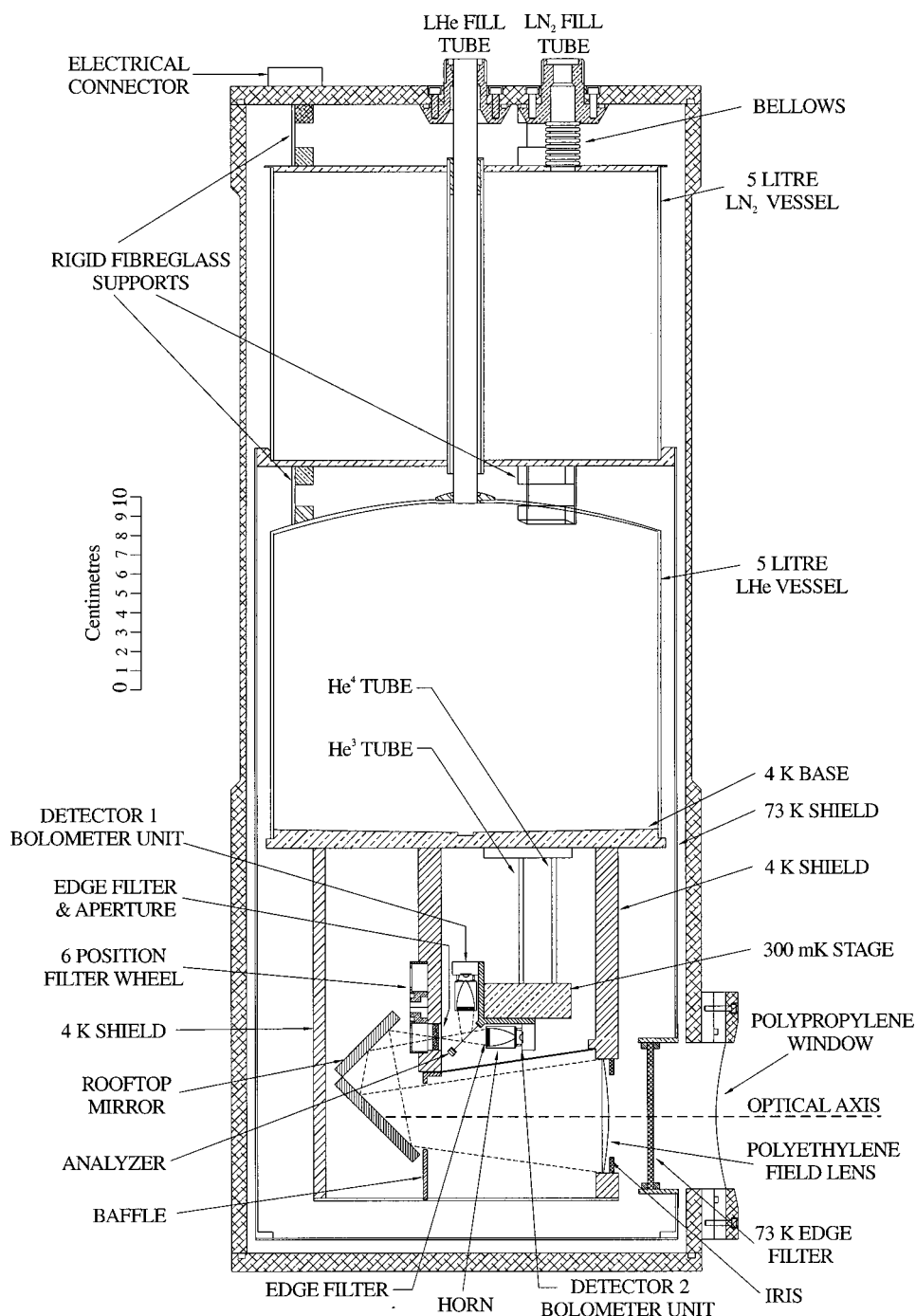
FIG. 1. Overview of the modified HDL8 Dewar configuration.

which reduces the formation of resonant optical cavities within the Dewar that produce unwanted channel spectra.[10] Mounted immediately behind the window on a liquid nitrogen (LN_2) shield is a large, ~75 mm diam, 35 cm^{-1} capacitive grid low pass edge filter.[11] This type of metal grid filter remains colder (and is therefore a less significant source of thermal emission) than absorption filters for two reasons: It efficiently reflects short wavelength radiation (rather than absorbing it) and, as a good thermal conductor, it is in better thermal contact with the LN_2 shield. The band pass filters are of similar construction, and are described in Sec. II B.

Following the light path into the Dewar, all the optics, from this point on, are cooled to the bulk liquid helium (LHe) bath temperature to reduce their thermal emission. An adjustable iris allows the optical beam to be matched to the diffraction limited telescope beam. Manual adjustment of the iris is made possible by a geared Torlon[12] shaft that passes to the outside of the Dewar via a high vacuum feedthrough. The shaft is hollow and loosely coupled to the external mechanism to minimize heat transfer. A 65 mm diam $f/3$ polyethylene planoconvex field lens, mounted directly behind the iris, re-images the telescope's primary mirror onto the detector units. The relatively long focal length of the field lens requires that the beam be folded by means of an aluminum dihedral (rooftop) mirror. The beam is then directed through one of the six filters in the filter wheel, a 33 cm^{-1} edge filter (wedge mounted to minimize optical resonances) and a polarizer (analyzer) mounted on the 300 mK stage. In this way
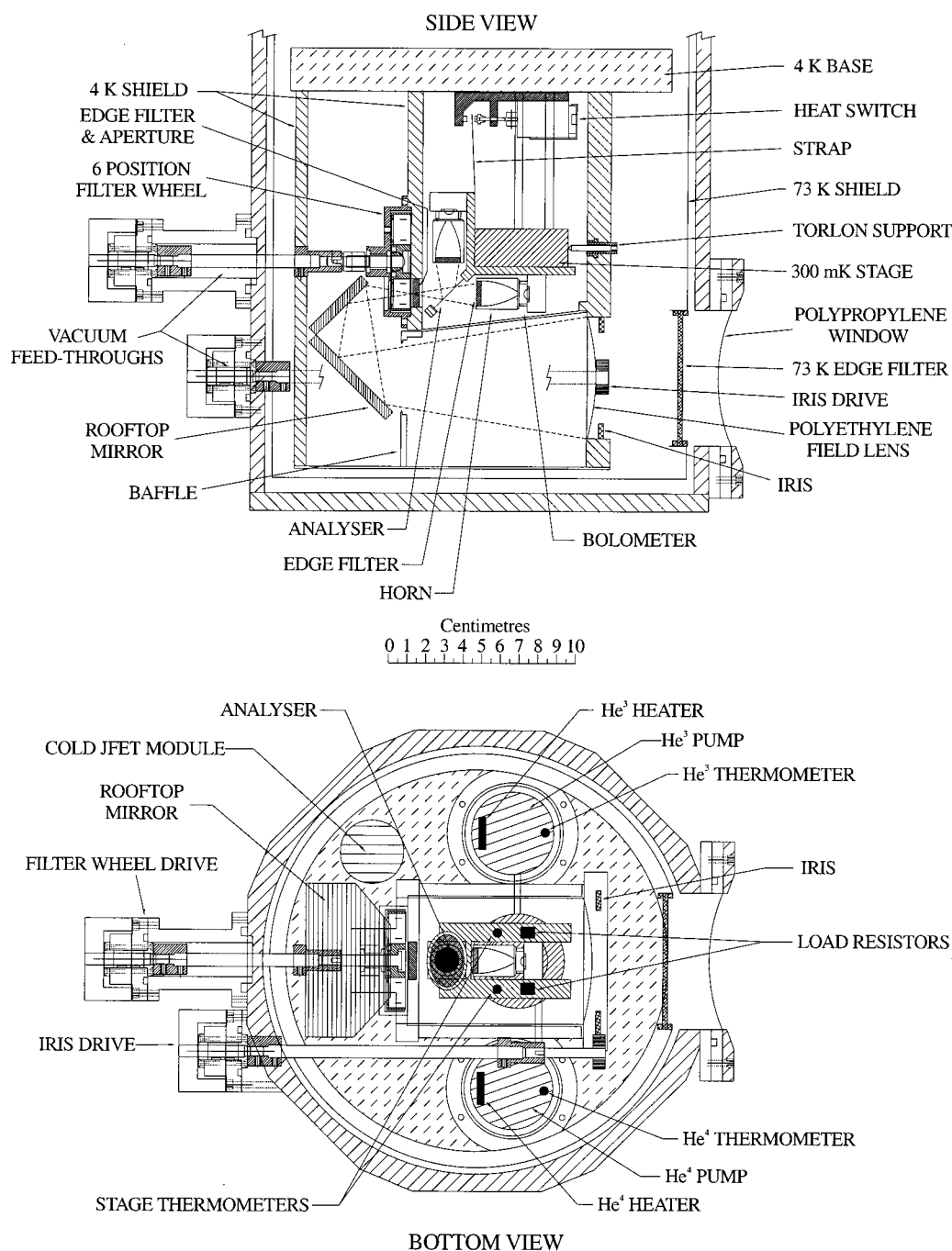
SIDE VIEW

4 K SHIELD
EDGE FILTER
& APERTURE
6 POSITION
FILTER WHEEL

VACUUM
FEED-THROUGHS

ROOFTOP
MIRROR

BAFFLE

ANALYSER

EDGE FILTER

HORN

4 K BASE
HEAT SWITCH
STRAP
73 K SHIELD
TORLON SUPPORT
300 mK STAGE
POLYPROPYLENE
WINDOW
73 K EDGE FILTER
IRIS DRIVE
POLYETHYLENE
FIELD LENS
IRIS

BOLOMETER

Centimetres
0 1 2 3 4 5 6 7 8 9 10

ANALYSER
COLD JFET MODULE
ROOFTOP
MIRROR
FILTER WHEEL DRIVE

IRIS DRIVE

STAGE THERMOMETERS

He³ HEATER
He³ PUMP
He³ THERMOMETER

IRIS

LOAD RESISTORS

He⁴ THERMOMETER
He⁴ PUMP
He⁴ HEATER

BOTTOM VIEW

FIG. 2. Detailed side and bottom views of the detector system.

the orthogonal components of the beam from the polarizing FTS are recombined and directed to two detector units.

Each detector unit consists of a Winston horn[13] which concentrates the radiation into an integrating cavity which houses the bolometer element. Each horn is capped by a low-pass, alkali-halide edge filter which prevents any stray radiation above 55 cm^{-1} from reaching the bolometers. The integrating cavities are machined from copper, and the horns are manufactured by electroplating copper onto precision ground, paraboloid mandrels. The integrating cavities and horns are gold plated to improve their reflectivity.

B. Filters

The filter wheel, shown in Fig. 2, holds six filters whose pass bands are matched to the atmospheric windows accessible from Mauna Kea, Hawaii. The pass bands are defined by a combination of resonant grid band pass filters and low-pass blocking filters. Manual selection of a particular filter is accomplished by a mechanical vacuum feedthrough similar to the one used for the iris adjustment with the exception that the external housing is elongated to allow for a longer Torlon drive shaft. Again, the shaft is hollow and loosely coupled at both ends to reduce thermal conduction to the 4 K filter

TABLE I. Filter characteristics.

Filter band	Low edge (cm^{-1})	High edge (cm^{-1})	Band center (cm^{-1})	Bandwidth (cm^{-1})
350s	28.82	29.89	29.36	1.07
350l	26.30	29.14	27.72	2.84
450	21.16	23.46	22.31	2.3
600	15.02	16.92	15.97	1.9
750	12.94	13.86	13.4	0.92
850	11.19	12.07	11.63	0.88
1100	8.66	10.23	9.445	1.57
1400	7.11	8.97	8.04	1.86

wheel, which would cause unwanted emission from the filters directly into the detector path. The filter wheel is held in position by detents on the wheel assembly, and connected to the LHe shield by a gold plated copper spring. Table I lists the characteristics of the available filters. Figure 3 shows the measured filter profiles superimposed on a model transmission spectrum for the summit of Mauna Kea. This model is for a precipitable water vapor amount of 0.5 mm, corresponding to very good observing conditions. The filters are well matched to the regions of high atmospheric transmission, thus minimizing variations in the flux received as the spectral width of the windows varies as a function of water vapor column abundance. In addition to reducing the thermal loading on the detectors, which increases their sensitivity, the filters also reduce the radiant heat load on the cryogenic system from the warm foreoptics, which extends the cryogen hold times. However, the greatest benefit lies in the fact that astronomical observations are less sensitive to variations in the spectral width of the atmospheric windows. This is of particular concern for a Fourier spectrometer and can result in a multiplex disadvantage.[14]

C. Bolometers

Sensitivities at or near the background limit can be achieved at millimeter wavelengths by composite bolometer detectors operating at 300 mK. Composite bolometers consist of a small semiconductor element, with a large temperature coefficient of resistance, mounted on a dielectric substrate. The dielectric substrate serves as the main absorber of the incident radiation, while the semiconductor element serves as the thermometer that measures the temperature fluctuations of the substrate. Since the frequency response of a bolometer increases as the heat capacity is reduced, it is advantageous to use a dielectric with low specific heat for the large surface area element which absorbs the radiation, and to make the bolometer crystal, with its intrinsically high specific heat, as small as possible. Furthermore, to ensure that the temperature measured by the bolometer element closely follows the fluctuations in the incident radiation, the thermal conductivity of the substrate must also be as high as possible. The detectors described in this article were designed to give optimum noise performance up to frequencies of ~100 Hz, corresponding to the infrared modulation frequencies produced by the FTS.

Figure 4 shows the design of the composite bolometers used in this detector. Each bolometer is constructed from a $(250 \mu m)^2 \times 275 \mu m$ crystal of nuclear transmutation-doped (Haller NTD material No. 13) Ge:Ga.[15] The crystal is mounted on a sapphire absorbing disk (3 mm diameter 30 μm thick). A bismuth film 100 nm in thickness is evaporated onto the rear of the sapphire disk to maximize the broadband absorption of incident radiation. The bolometer is suspended in an integrating cavity by two Pyrex rods (14 μm diameter 0.65 mm long) that provide stiff support, ensuring that any microphonic vibration of the element will occur at a frequency well above the modulation frequencies produced by the FTS. Two sides of the crystal are boron ion implanted and palladium and gold plated to provide a good thermal and electrical connection with the two brass wires (12 μm diameter 2.5 mm long) which form the electrical connection to the crystal. The bolometer is connected to the rest of the circuit with 80 μm Manganin wire. The brass wires, quartz standoffs, and to a lesser extent the Pyrex rods define the thermal conduction path to the integrating cavity housing, which operates at a temperature of 300 mK.

The largest contributions to the heat capacity arise from the bolometer element itself, the brass wires, and the conduc-
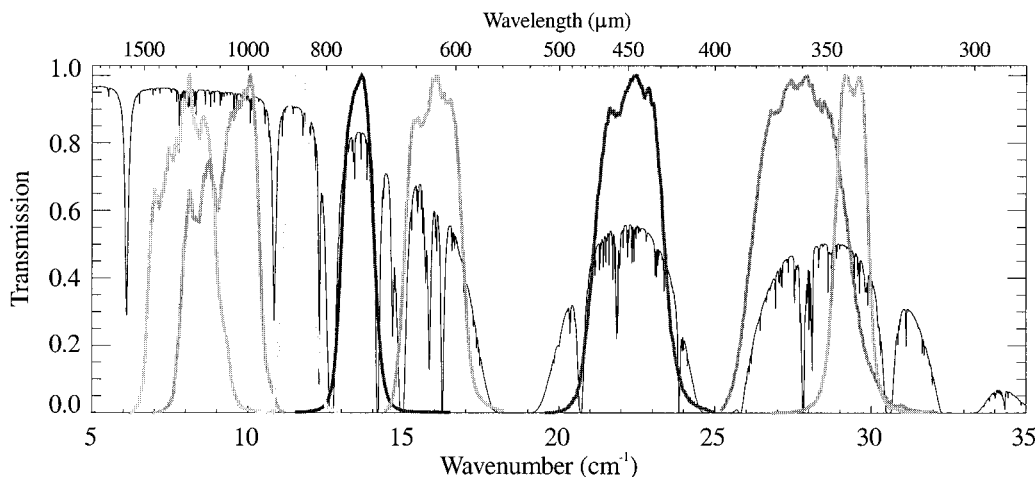

FIG. 3. Available filter bands (Table I) overlaid on a theoretical atmospheric transmission spectrum modeled for Mauna Kea with 0.5 mm precipitable water vapor.
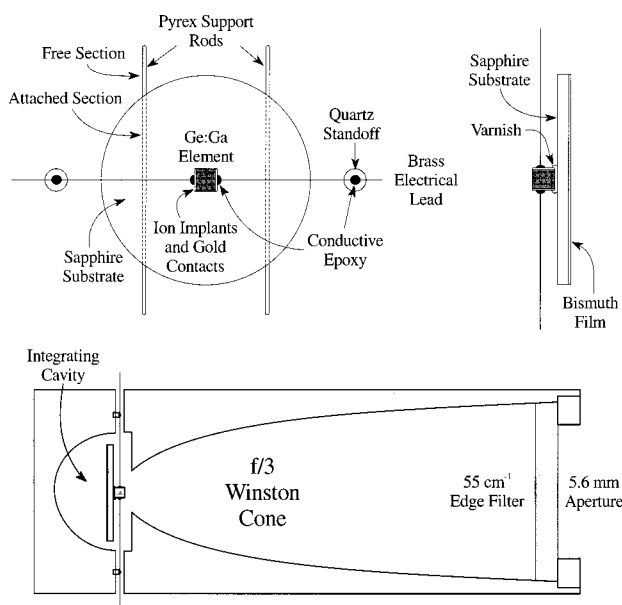
FIG. 4. Detailed view of the composite bolometer construction (top) and of the bolometer unit integrated with the Winston cone (bottom).

tive epoxy used to bond the wires to the gold contacts. The dimensions of these components are optimized by considering the following. The bolometer element can only be made smaller at the expense of lower resistance, and hence a lower bias voltage change for a given temperature change, the brass wires need to be thick enough to create a large thermal conductivity, and the epoxy droplets must be large enough to ensure good thermal and electrical bonds. The main uncertainty in determining the total heat capacity during fabrication is due to the difficulty in measuring precisely the volume of varnish used in bonding the crystal to the substrate and of the epoxy forming the electrical connections. The design values of the heat capacity and thermal conductivity of these detectors, $C = 35$ pJ/K and $G = 20.5$ nW/K, respec-

tively, have been chosen to optimize the frequency response and sensitivity of the detectors.

D. Cryogenic system

The cryostat, shown in Figs. 1 and 2, contains a LN_2 and a L^4He tank, each with a capacity of 5 ℓ. A LN_2 cooled radiation shield provides an intermediate temperature buffer. Two radiation shields, connected to the L^4He base plate, surround the closed cycle, dual stage ^{4}He–^{3}He refrigerator which cools the detector stage to 300 mK.[16] This system offers several advantages over externally pumped refrigerators: it is compact, does not require an external mechanical pump and is thus free of vibrations, and is easily recycled under computer control.

The detector stage consists of two concentric and connected vessels, shown schematically in Fig. 5. The outer one contains 5 standard temperature and pressure (STP) ℓ of ^{4}He gas at ~6 MPa, the inner one contains 3 STP ℓ of ^{3}He gas at ~6 MPa. Each is connected to a separate charcoal adsorption pump via short, thin-walled stainless steel tubing. Additional support is provided to the stage by two hollow Torlon rods that prevent vibration. The pumps themselves are connected to the base plate of the bulk L^4He tank by silver wires whose dimensions determine the thermal conduction path, and, therefore, the pumping rate for each pump.

Initially, the Dewar is filled with cryogens and the thermal strap is engaged to provide a link between the bulk L^4He reservoir and the stage (Fig. 2). The thermal link is actuated by a latching solenoid which grips a gold plated copper finger that extends down from the stage. (The stage is so well isolated that without this measure it would take several days to reach 4 K.) During the development phase it was found that the field strength of the solenoid magnet decreased over time, which in turn required a higher, and unacceptable, latching current. This problem was traced to the demagnetization of the ferromagnet that occurred as the coil was re-
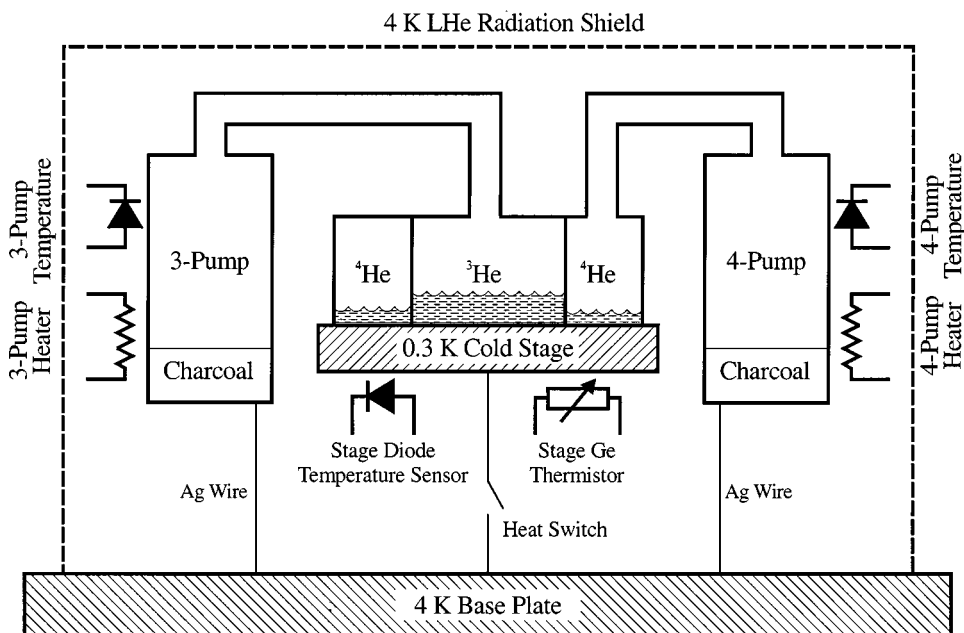

FIG. 5. Schematic of the ^{4}He–^{3}He cryogenic system, showing the adsorption pumps, the heaters, thermometers, and thermal links. The operation of the ^{4}He–^{3}He refrigerator is discussed in detail in the text.
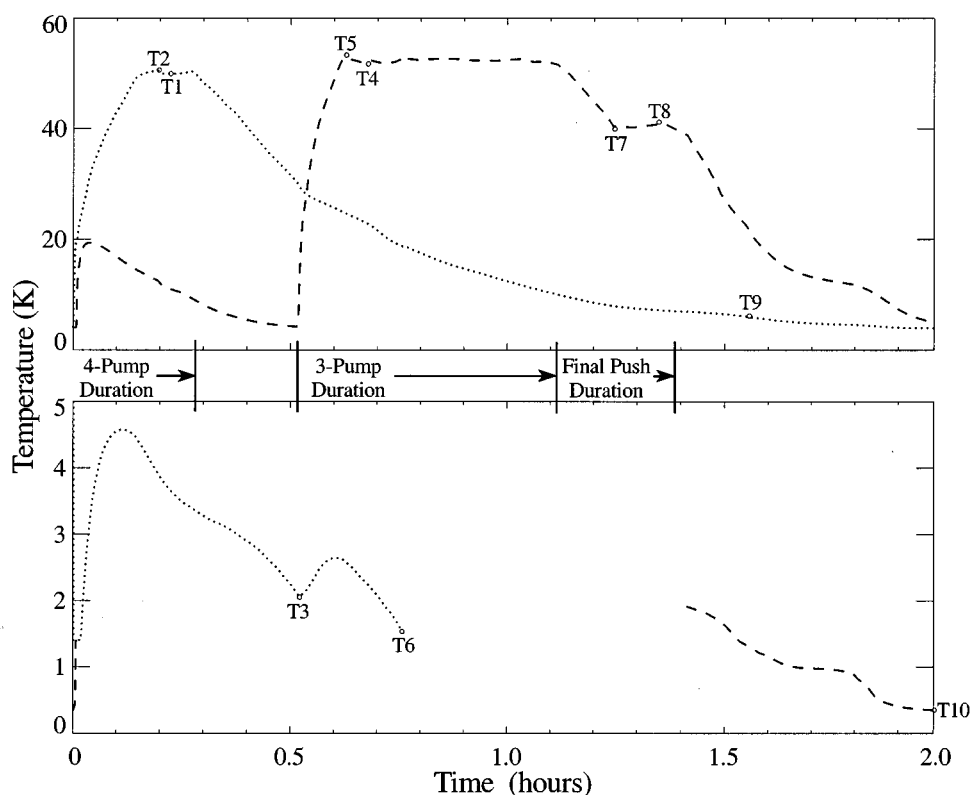
FIG. 6. Typical recycling log showing the operation of the ^{4}He and ^{3}He pump cycles. Key temperature set points are indicated by $T1$–$T10$ and are discussed in detail in the text. The refrigerator can be recycled in under 2 h and has a hold time in excess of 30 h under normal operating conditions.

peatedly energized. Replacement with a samarium–cobalt magnet has solved this problem.

A laptop computer, interfaced to a cycling electronics module, automatically recycles the cryogenic system using a simple algorithm, described below, to control the pump heaters as a function of temperature and time. Temperature measurements are provided by four thermometers, one mounted on each pump and two mounted on the stage. Three of these are diodes designed for measurements above 1 K [DT470 (Ref. 17) or the equivalent], and one is a Ge sensor [GRT-100 (Ref. 17)] which is mounted on the stage and designed to measure temperatures in the 300 mK range. The heaters (2 W) are attached to the sides of each pump far from the thermometers.

E. Cryogen recycling procedure

A typical recycling log is shown in Fig. 6 where key temperature control points are indicated. At $t=0$ h the ^{4}He pump heater is turned on and gas is driven out of the charcoal pump and into the outer collecting vessel where it condenses, since it is below the critical temperature of 5.2 K for ^{4}He. The temperature of the ^{4}He pump is held between the set points, $T1$ and $T2$, providing a hysteresis of $\sim$1 K. (Since there was still some L^{3}He left in the system, it is seen in Fig. 6 that the temperature of the ^{3}He pump increases as it does work.) When all of the ^{4}He gas is liquefied, the heater is turned off and the pumping action of the ^{4}He pump begins. Since there is no direct indication of when all the ^{4}He has liquefied (except for a decrease in the slope of the stage temperature curve due to the reduction in flow of hot ^{4}He gas), the heater is turned off after a set time ($\sim$20 min at $t=0.3$ h).

When the action of the ^{4}He pump has lowered the temperature of the cold stage to below the critical temperature of 3.3 K, ^{3}He will start to condense in the inner vessel and the ^{3}He pump heater can be activated. In practice, $T3$, the stage diode temperature at which the ^{3}He pump is turned on, is set at 2.2 K to allow the ^{4}He pump to extract as much heat from the stage as possible without allowing the L^{4}He to become superfluid. The temperature of the ^{3}He pump is held between set points $T4$ and $T5$ providing a hysteresis of $\sim$1 K. The heat of the incoming ^{3}He gas and the latent heat of vaporization as the ^{3}He liquefies raise the temperature of the stage slightly which increases the boil-off rate of the L^{4}He in the outer vessel. This can be seen in Fig. 6 from the rise in the stage diode temperature at $t=0.6$ h and the change in slope of the ^{4}He pump temperature. It is critical that all the L^{4}He is evaporated before the ^{3}He pump heater is turned off, or too much L^{3}He will be wasted by cooling the L^{4}He bath. There is also the possibility that the remaining L^{4}He will be cooled below its superfluid transition temperature, creating a potential heat flow problem due to the resulting superfluid flow. To ensure that all the L^{4}He has evaporated, the temperature of the ^{3}He pump heater is reduced to a lower level at 1.2 h to ensure that all the L^{4}He is removed from the stage before the final cooldown. This extra time is set to 30 min or until the temperature of the ^{4}He pump falls below a set temperature, $T9$ (6 K). At $t=1.4$ h the ^{3}He pump heater is turned off and the action of the ^{3}He pump lowers the temperature of the stage. Finally, at $t=2$ h the stage reaches its operating temperature of 300 mK. At the end of the automatic cycling process, power to the temperature sensors is cut off to prevent unnecessary loss of L^{3}He, and power to the cycle box is
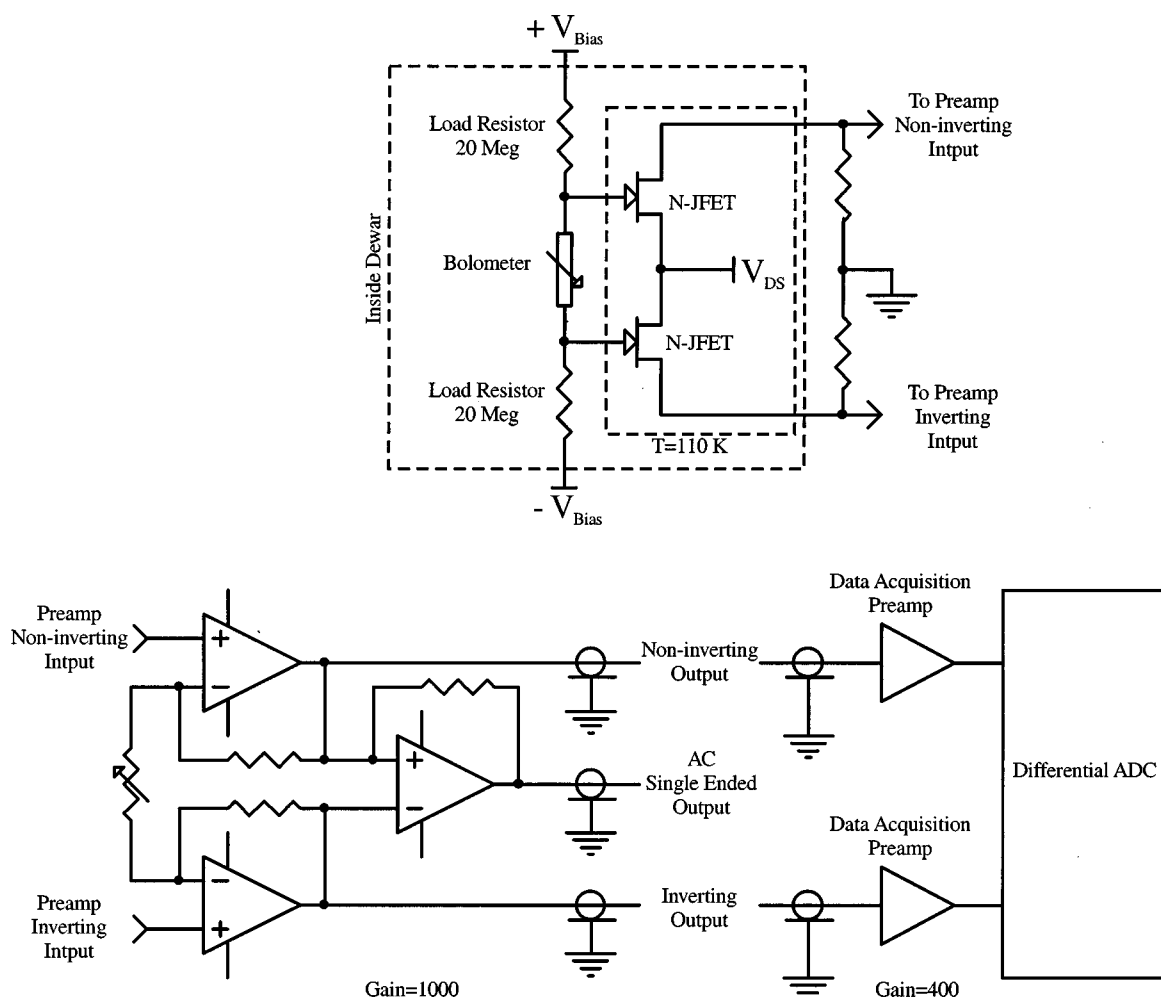
FIG. 7. Schematic of the fully differential electronic design. The top diagram shows the cold electronics: bolometer and load resistors (300 mK) and the JFETs (110 K). The bottom diagram shows the ambient differential preamplifier, line driver, receiver, and ADC.

also cut off to prevent any possible accidental reactivation of the pumps or heat switch.

Recycling the detector system at the JCMT takes 2 h and consumes 0.9 ∕ of bulk L^{4}He and a negligible amount of LN$_2$. Once cycled, the system has a L^{3}He hold time in excess of 30 h. In practice, the bulk cryogens are replenished at the end of an observing shift and the automatic recycling software is scheduled to run 3 h prior to the beginning of the observing shift on the next day.

F. Electronic design

Environmental noise is often difficult to quantify since it includes all external sources of noise. Of these, microphonics and electromagnetic interference (EMI) are the most significant. The telescope presents a hostile environment. Large currents in the telescope drive give rise to large and variable magnetic fields. Noisy compressors are periodically activated. The grounding network is not particularly good in the small signal sense, with common mode voltages of the order of volts often present between the telescope frame and the scientific instrumentation. Since previous attempts to eliminate the environmental noise component met with limited success, a new approach was used for this detector system.

The microphonic sensitivity of the system has been partly addressed in the mechanical construction of the cold stage and the mounting of the detector elements. To ensure that induced currents are not generated in the presence of magnetic fields, all wiring inside the Dewar is formed of twisted pairs and is varnished down to the Dewar structure. The principal remaining concern is the reduction of EMI. To reduce EMI associated with electric fields, the preamplifier is mounted in a radio frequency interference (RFI) shielded box mounted to the side of the Dewar. The power supply for the preamplifier and bolometer bias network is contained inside this box. The Dewar provides a shield for the detectors. Together, the Dewar and the preamplifier can be considered to be within a single, shielded enclosure.

The novel feature of this detector system, and possibly the most significant factor in its performance, is the fully differential design of the detector, preamplifier, and data acquisition electronics. Several low noise preamplifiers for far-infrared bolometers and photoconductors have been presented in literature,[18–20] but none uses the fully differential design described here. In a balanced differential system, any noise component induced in one signal line will be matched by an identical component induced in the other signal line. Upon taking the difference between the two signal lines, the
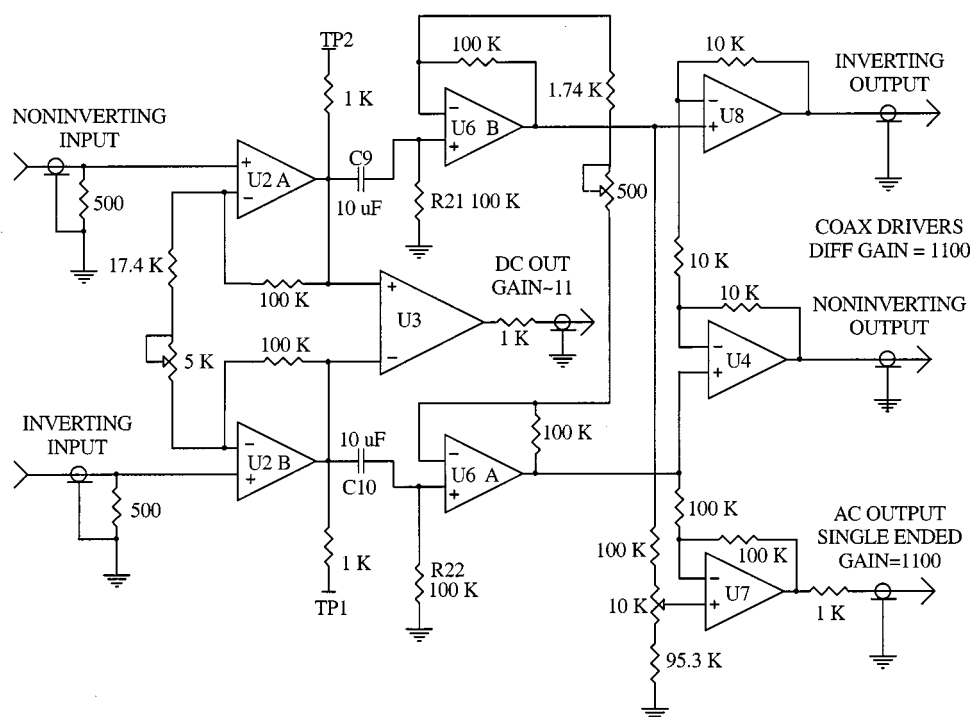
FIG. 8. Schematic of the preamplifier design for one detector.

interference components will cancel each other, leaving the desired differential signal from the detector element. However, this technique will only work if the entire detector system is completely symmetrical. Figure 7 shows a schematic of the symmetrical electronic design developed for these detectors. In this design, a bolometer element is isolated from the Dewar ground and placed between two identical bias resistors and two identical and complementary active bias voltage generators. The cold preamplifier uses matched JFETs (IFN146),[21] configured as source followers, fed by a common drain voltage (4.96 V). The room temperature preamplifier consists of two identical channels, one for the inverting output and one for the noninverting output. It is essential that the gains and phase shifts of the two channels are the same. Since the data acquisition system is located in the control room of the JCMT, a 30 m twisted pair, shielded cable connects the differential output of the preamplifier with a balanced differential line receiver designed to ensure that the complex impedances seen by the inverting and noninverting signal lines are the same. Finally, the output of the line receiver is connected to a 16-bit differential analog-to-digital converter (ADC).

Figure 8 shows a schematic diagram for one channel of the detector preamplifier. The preamp is essentially a two stage instrumentation amplifier used to amplify the small differential signal across the bolometer element and reject common-mode noise. The input stage formed by the matched op-amps in U2 (LT1124) provides a differential gain of 11 (in addition to the JFET gain of $\sim$0.89), while maintaining a unity common-mode gain. The dc output op-amp, U3 (AD620), removes any remaining common-mode noise and provides a single ended output representing the dc voltage across the bolometer element with a gain of 10. Similarly, the second stage of the preamp, consisting of U6 and U7 (OP297) with a gain of 100, produces a single ended ac

output with a total gain of 1000. U4 and U8 (AD811) are unity gain differential line drivers which send the inverted and noninverted signals (with a gain of 1000) to the data acquisition system. The electrical RC filters formed by C9 and R21 and by C10 and R22 define the frequency response of the preamp and provide a high-pass cutoff frequency of 0.16 Hz in order to decrease $1/f$ noise without affecting the detector signal. The net preamp noise contribution is discussed with the system noise analysis in Sec. III.

Care was taken in the electronics design to minimize noise levels. The JFETs were chosen for their extremely low noise characteristics. The input op-amps were selected for their high common-mode rejection ratio (CMRR) of 120 dB and their low input noise voltage and current densities of 3 nV/$\sqrt{\text{Hz}}$ and 1.3 pA/$\sqrt{\text{Hz}}$, respectively, at 10 Hz. The load resistors were mounted to the 300 mK cryogenic stage in order to minimize their Johnson noise contribution. Also, low noise, active bias voltage generators were used instead of batteries to supply the bias current through the bolometers, since experience showed that batteries introduced additional noise. A schematic of the circuit for one detector is given in Fig. 9.[22] Low noise op-amps (input noise voltage density=3.6 nV/$\sqrt{\text{Hz}}$ and input noise current density $= 1.1\, nV/\sqrt{\text{Hz}}$ at 10 Hz) produce a symmetrical positive and negative bias voltage across the load resistor network, with a total effective noise voltage density across the bolometer of $\sim$0.2 nV/$\sqrt{\text{Hz}}$ at 10 Hz. A temperature compensated current source is used to generate the input voltage for the op-amps to ensure that the bias voltage does not vary due to the frequent temperature fluctuations in the telescope's dome.

The efficacy of the differential electronics design is illustrated in Fig. 10 which shows the average of 20 spectra, obtained with the FTS, from one of the SCUBA[23] pixels (which use a single-ended design) compared to a single spectrum obtained with one of the detectors described in this
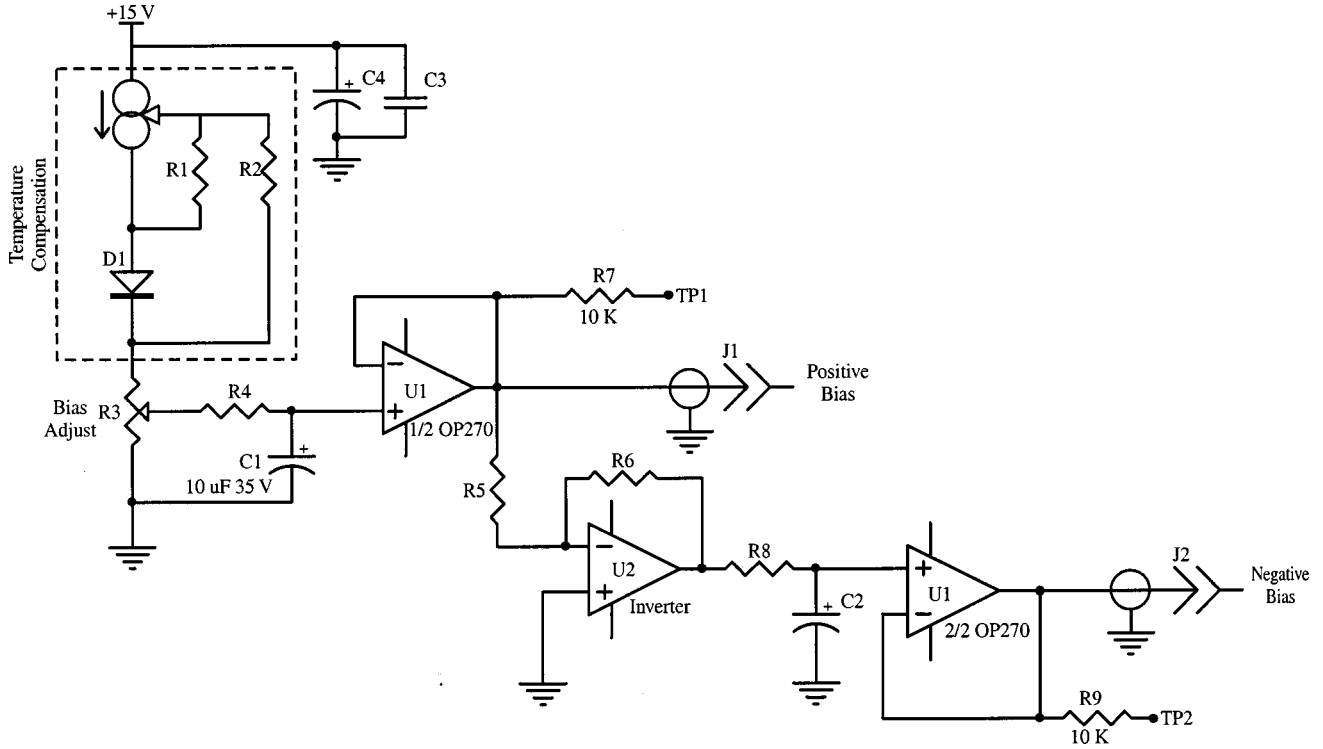
FIG. 9. Schematic of the low noise, bipolar bias voltage generator.

article. In this comparison, the FTS, detector filter band (850 μm), calibration sources, and processing are identical. The spectra cover the range of 0–70 cm^{-1} (0–140 Hz). The more sensitive SCUBA spectrum shows many interference features, in stark contrast to that obtained with the differential amplifier design presented in this article, which shows essentially a white noise spectrum with a small feature at 60 Hz (30 cm^{-1}).

III. NOISE ANALYSIS

The factors to be considered in the preamplifier design are the electronic and environmental noise levels and the required speed of response. The response time is determined by the time constant of the detector, ~30 ms, a condition that is easily met. The environmental noise is of greatest concern. The noise performance of the preamplifier is based on the total system noise voltage density, N_{sol}, given by

$$N_{\text{tot}} = \sqrt{N_{\text{bol}}^2 + N_{\text{preamp}}^2 + N_{\text{bias}}^2 + N_{\text{env}}^2}, \tag{1}$$

where N_{bol} is the bolometer noise, N_{preamp} is the preamplifier noise, N_{bias} is the bias network noise, and N_{env} is the environmental noise, each in nV/$\sqrt{\text{Hz}}$. With a well designed electronics system, the bolometer noise will be dominant. The goal then is to reduce the nonbolometer noise source sum to less than one half the bolometer noise.

$$N_{\text{preamp}}^2 + N_{\text{bias}}^2 + N_{\text{env}}^2 \leq \left(\frac{N_{\text{bol}}^2}{2} \right)^2. \tag{2}$$

When equal, this represents a 12% increase in system noise and thus an increase of 25% in the time required to achieve a given signal to-noise (S/N) ratio.

The noise model of the bolometer, bias network, and preamplifier is shown in Fig. 11(a). The noise generators shown in Fig. 11 are discussed below.

A. Preamplifier noise contribution

The noise model of the amplifier input stage may be reduced to that shown in Fig. 11(b). The current and voltage sources are referred to as the input of the amplifier. Given the bolometer resistance, R_{bol}, and the bias load resistance, R_L, the effective preamp noise, N_{preamp}, due to the preamplifier input noise current, $i_{n\text{preamp}}$, and noise voltage, $e_{n\text{preamp}}$, is given by

$$N_{\text{preamp}} = \sqrt{e_{n\text{preamp}}^2 + \left(i_{n\text{preamp}} \frac{R_L R_{\text{bol}}}{R_L + R_{\text{bol}}} \right)^2}. \tag{3}$$

The load resistance, R_L, is 40 MΩ, and the bolometer resistance, R_{bol}, is typically ~3.5 MΩ. $e_{n\text{preamp}}$ and $i_{n\text{preamp}}$ depend on the preamplifier input design and, in particular, on the active device parameters. The high resistance of the bolometer necessitates an input device with low input noise current. For this reason a JFET was chosen. The input noise voltage for a JFET is given by

$$e_{n\text{JFET}} = \sqrt{4kTR_N}, \tag{4}$$

where k is Boltzmann's constant, T is the temperature, and $R_N \approx 0.67/g_{fs}$ is the equivalent noise resistance of the JFET (g_{fs} being the forward transconductance of the device). $e_{n\text{JFET}}$ can be reduced by increasing the forward transconductance (equivalent to increasing the gate area) and/or decreasing the device temperature. The limit to performance enhancement is determined by the increased input capacitance and the decreased carrier mobility at low temperature.
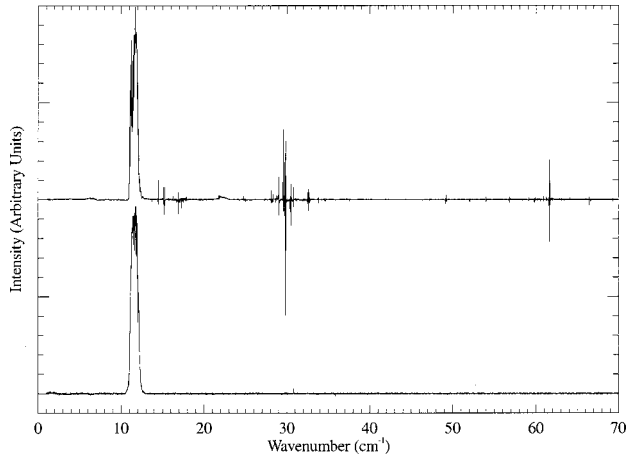
FIG. 10. Comparison of a calibration spectrum measured with the detector presented in this article (lower trace) with the average of 20 calibration spectra obtained using one of the SCUBA pixels (upper trace), taken under identical conditions. The wave number scale shown is one half of the electrical frequency scale (i.e., 30 cm^{-1} is equivalent to 60 Hz). The power of the differential circuit in eliminating electrical interference is readily apparent.
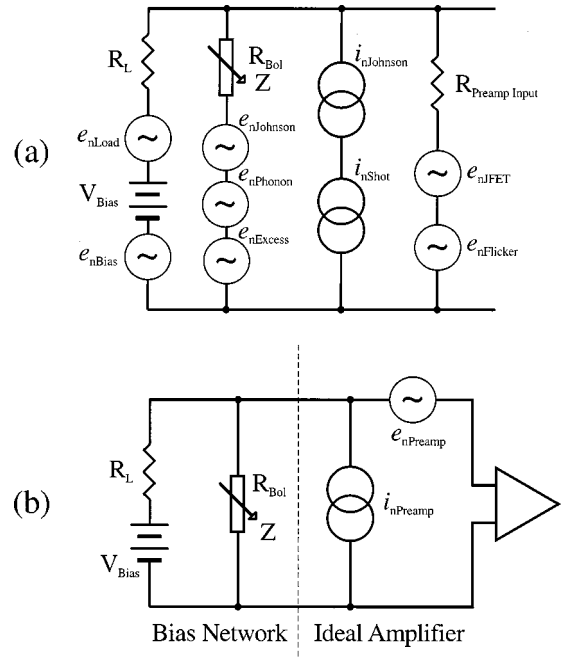

FIG. 11. (a) Schematic of all the noise generators present in the electronics system. (b) A simplified schematic of the preamplifier noise generators in terms of the equivalent input current and voltage noise.

There are two components to the noise current. The thermal component is given by

$$i_{n\text{Johnson}} = \sqrt{\frac{4kT}{R_{GS}}}, \tag{5}$$

where R_{GS} is the gate–source resistance. The shot component of the noise is given by

$$i_{n\text{shot}} = \sqrt{2qI_G}, \tag{6}$$

where q is the electronic charge and I_G is the reverse gate current. In order to minimize the input noise current it is necessary to minimize the reverse gate current. Two parameters affect the gate current: the reverse junction potential, V_{DS}, which must be minimized to be just slightly greater than the pinchoff voltage of the JFET, and the operating temperture of the JFET. Since the current is a strong function of device temperature, the JFETs are operated at $T \sim 100$ K to further reduce the noise current.

Two additional sources of noise must be considered: Flicker noise, generally attributed to surface defects in the device,

$$e_{n\text{flicker}} \approx \sqrt{4kTR_N \frac{f_1}{f^n}}, \tag{7}$$

where f_1 is the corner frequency and $1 \leq n \leq 2$, and popcorn noise, which is caused by contamination during device production. Both sources of noise can be minimized by careful selection of the manufacturer and the fabrication process.

Based on the above considerations, IFN146 JFETs were selected for the input stage of the preamplifier. At operating temperature the JFET reverse gate current, I_G, is ~0.5 pA and its transconductance, g_{fs}, is 0.035 S.

The flicker noise component of the IFN146 has a relatively high corner frequency, f_1, of 1 kHz. The total noise voltage at any frequency can be expressed by combining Eqs. (4) and (7) as

$$e_{n\text{preamp}} = \sqrt{4kTR_N \left(1 + \frac{f_1}{f^n}\right)}. \tag{8}$$

The total preamp noise current can be expressed by combining Eqs. (5) and (6) as

$$i_{n\text{preamp}} = \sqrt{\frac{4kT}{R_{GS}} + 2qI_G}. \tag{9}$$

The total preamplifier noise contribution at a modulation frequency of 50 Hz from Eq. (3) then become $N_{\text{preamp}} \approx 1.5$ nV/$\sqrt{\text{Hz}}$.

B. Bias network noise contribution

The Johnson noise in the bias resistor (see Fig. 5) mounted on the 300 mK stage is

$$e_{n\text{load}} = \sqrt{4kTR_L} = 26 \text{ nV}/\sqrt{\text{Hz}}. \tag{10}$$

However, since the bias resistor and detector form a voltage divider, only a portion of this noise voltage, equal to 2.1 nV/$\sqrt{\text{Hz}}$, appears across the detector. While batteries have customarily been used to provide low noise power for the bias network, it has been our experience that they contribute an additional source of noise. For this reason a low noise active bias generator has been designed which contributes a negligible additional 0.2 nV/$\sqrt{\text{Hz}}$, bringing the total bias network noise contribution, N_{bias}, to 2.1 nV/$\sqrt{\text{Hz}}$.

C. Bolometer noise contribution

The noise sources in the bolometer element are Johnson noise, phonon noise, shot noise, and flicker noise. The shot and flicker noise produced in the bolometer contacts is difficult to model, and is measured as excess noise, $e_{n\text{excess}}$, in the detector signal. The total bolometer noise contribution is

$$N_{\text{bol}} = \sqrt{e^2_{n\text{Johnson}} + e^2_{n\text{phonon}} + e^2_{n\text{excess}}}. \tag{11}$$

The Johnson noise produced in the bolometer is given by

$$e_{n\text{Johnson}} = \sqrt{4kTR_{\text{Bol}}}, \tag{12}$$

where T is the temperature of the bolometer element, which varies with the power load but is typically $\sim$370 mK.

Fluctuation in heat flow through the bolometer thermal links produces a phonon noise voltage:[24]

$$e_{n\text{phonon}} = 2T\mathfrak{R}\sqrt{kG}\left[1 - \left(\frac{\beta}{2} + 1\right)\Delta \right.$$
$$\left. + \left(\frac{(\beta+2)(3\beta+2)}{12}\right)\Delta^2 - \dots\right]^{1/2}, \tag{13}$$

where G is the thermal conductance of the links, T is the bolometer temperature, $\mathfrak{R}$ is the detector responsivity (V/W), β is a material-dependent parameter of the links ($\beta = 1$ for the brass wires), and $\Delta = 1 - T_0/T$, where T_0 is the bolometer housing temperature ($\sim$290 mK). At a bias current of 30 nA, the phonon noise is $\sim$8.5 nV/$\sqrt{\text{Hz}}$. The total bolometer noise contribution from Eq. (11) is $\sim$12.0 nV/$\sqrt{\text{Hz}}$, bringing the total estimate of the system noise, N_{tot}, to $\sim$12.3 nV/$\sqrt{\text{Hz}}$.

IV. MEASURED DETECTOR PERFORMANCE

Measurements of the bolometer voltage as a function of bias current and radiant power loading on the element provide a simple method by which to characterize the performance of the detector.[24] Analysis of the resulting $V-I$ curves allows the noise equivalent power (NEP) to be calculated as a function of bias, which in turn determines the optimum bias current for a given loading condition. Theoretical modeling of the $V-I$ curves yields values for parameters such as the thermal conductance and the optical efficiency that would otherwise be difficult to measure.

The bolometer voltage was recorded as the bias current was scanned over the range of 0–100 nA. Data were collected for both bolometers that were viewing a blanked off filter position ($\sim$4 K), corresponding to the least possible radiant power loading. An IDL[25] procedure was written to fit the theoretical $V-I$ equations. In this analysis the bath temperature, T_0, thermal conductance, G_0, radiant loading, Q, and amplifier gain were free parameters. The minimum χ^2 in this four-dimensional space determined the parameters for the best model fit.

The $V-I$ data and model are presented in Fig. 12. The upper graph shows theoretical fits (solid lines) to the measured $V-I$ curves (dots) for detector 1 that is viewing a blanked off filter at $T \approx 4$ K, representing the closest to ideal (zero power loading) behavior. The lower graph shows the corresponding data and theoretical fit for detector 2. For detector 1, an analysis yields best fit parameter values of $G_0 = 23.5$ nW/K, $T_0 = 294$ mK, and $Q = 89$ pW. The corresponding values for detector 2 are $G_0 = 19.4$ nW/K, $T_0 = 290$ mK, and $Q = 157$ pW.
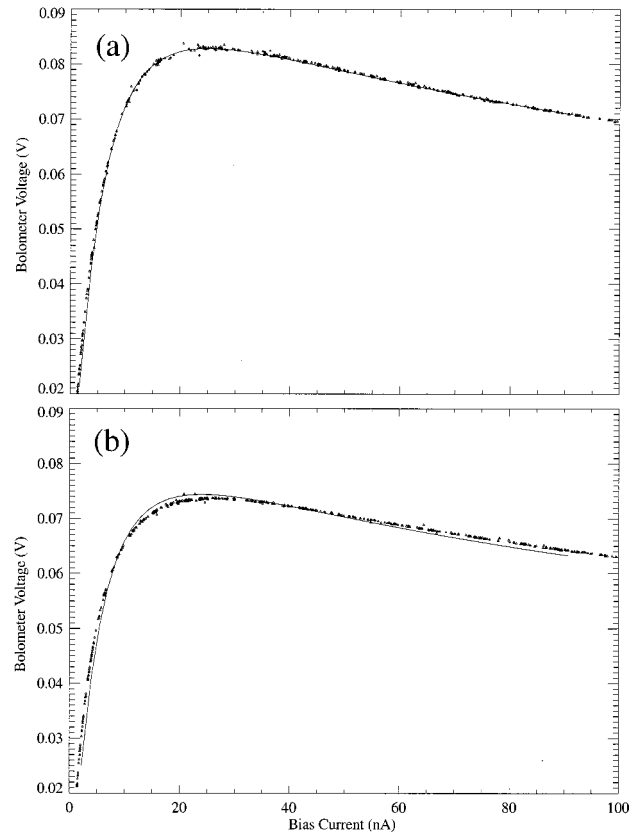

FIG. 12. Measured $V-I$ data (symbols) and the best fit of the theoretical model (lines) for the blanked off filter position for (a) detector 1 and (b) detector 2.

$V-I$ data were also recorded for both detectors that viewed LN$_2$ (73 K), ambient (290 K), and hot (330 K) blackbody sources in all six filter bands in order to calculate the detector responsivity.

A. Theoretical minimum NEP

The minimum noise level that can be achieved by the detector system is the intrinsic noise of the bolometers, which consists of Johnson noise from the bolometer resistance and phonon noise arising from fluctuations in heat flow between the bolometer and the heat sink. This theoretical minimum NEP can be expressed as[26]

$$\text{NEP}_{\text{theory}} = aT_0\sqrt{kG_0} + bQ\sqrt{\frac{k}{G_0}}, \tag{14}$$

where a and b are parameters of the bolometer. For the bolometers used in this system, $a = 2.52$ and $b = 3.31$, yielding a theoretical NEP of 4.3×10^{-16} W/$\sqrt{\text{Hz}}$ for detector 1 and 3.9×10^{-16} W/$\sqrt{\text{Hz}}$ for detector 2. This model does not include environmental or photon noise. The experimentally derived NEP values are discussed separately below and are summarized in Table II.

B. Measured electrical NEP

The detector electrical NEP can be determined from the electrical responsivity using the relation

TABLE II. NEP.

NEP calculation	Detector 1 $\times 10^{-16}$ W/Hz	Detector 2 $\times 10^{-16}$ W/Hz
Optical NEP (Q/S/N)	10.8	5.4
NEP (noise/responsivity)	5.6	3.5
NEP (spectral analysis)	10.2	7.2
Theoretical minimum NEP	4.5	4.1

$$\text{NEP}_{\text{electric}} = \frac{N_{\text{tot}}}{\mathfrak{R}}, \tag{15}$$

where N_{tot} is the noise voltage and $\mathfrak{R} = dV/dQ$ is the dc electrical responsivity (V/W). The responsivity as determined from the analysis of Mather[24] can be expressed as

$$\mathfrak{R} = \frac{R_L}{2IR_{\text{bol}}} \frac{Z - R_{\text{bol}}}{Z + R_L}, \tag{16}$$

where I is the bias current and $Z = dV/dI$ is the dynamical impedance of the bolometer. Alternatively, the responsivity may be obtained directly by measuring the voltage difference between two V–I curves corresponding to a known difference in radiant power loading. Noise values were obtained using a spectrum analyzer. For typical operating bias currents ($\sim$30 nA) the responsivity is the order of 20 MV/W, and the measured noise voltages at 70 Hz are $\sim$12 nV/$\sqrt{\text{Hz}}$ for detector 1 and $\sim$6 nV/$\sqrt{\text{Hz}}$ for detector 2. This approach yields minimum electrical NEP values of 5.6×10^{-16} and 3.5×10^{-16} W/$\sqrt{\text{Hz}}$ for detectors 1 and 2, respectively.

C. Measured optical NEP

A standard method of determining the optical performance of a detector is to measure the modulated signal, S, produced by a rotating chopper as the detector alternately views sources of different temperatures, and compare this with the noise, N, measured with the detector viewing the individual sources. The optical NEP of the system is then given by

$$\text{NEP}_{\text{optical}} = \frac{P_{\text{incident}}}{\text{S/N}}. \tag{17}$$

P_{incident} is the root mean square (rms) chopped radiant power incident on the detector, as determined from the source temperatures and the throughput. Using this method yields optimum $\text{NEP}_{\text{optical}}$ values of 10.8×10^{-16} and 5.4×10^{-16} W/$\sqrt{\text{Hz}}$ for detectors 1 and 2, respectively. It is not clear why these NEP values are higher than those derived above but it may be due to differences between the dc and ac optical responsivities of the detectors or possibly to errors in the estimate of the throughput.

D. Measured spectral NEP

The blackbody calibration spectra Sec. IV described in were analyzed to determine the NEP of the detector–FTS system. For a FTS, the S/N in a spectral element is related to the detector NEP by Eq. (18),[27] where P is the power in a spectral element, and T is the integration time of the interferogram.
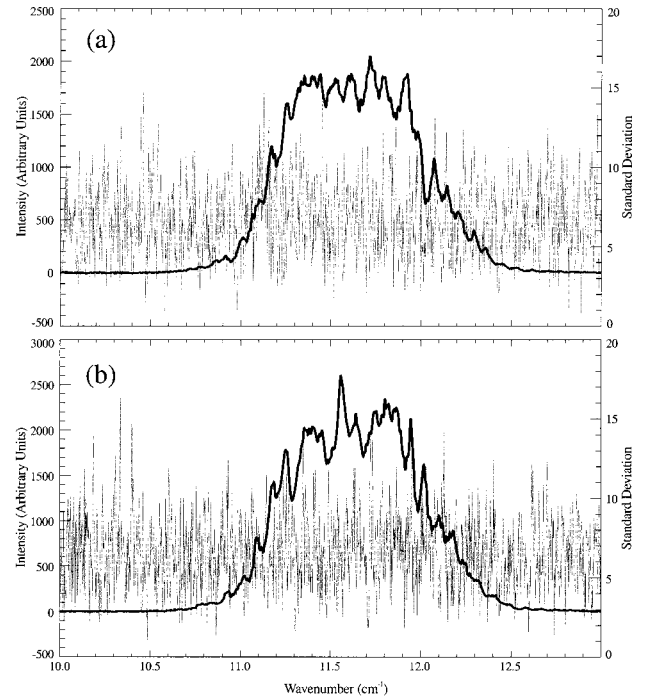

FIG. 13. Average of six calibration spectra (thick lines) and the standard deviation in each resolution element (thin lines) for the 850 μm band for detector 1 (a) and detector 2 (b).

$$\text{S/N} = \frac{P}{\text{NEP}_{\text{spec}}} \sqrt{\frac{T}{4}}. \tag{18}$$

Since the power from a blackbody source is related to the temperature through the Planck function, Eq. (18) can rewritten in terms of the NEP at the bolometer[27] in Eq. (19), where N is the number of averaged interferograms, ΔT is the 1σ rms temperature error in a 150 MHz bandwidth, and ϵ is the total detector system efficiency.

$$\text{NEP}_{\text{spec}} = 5.67 \times 10^{-14} \sqrt{N} \Delta T \times \epsilon. \tag{19}$$

Figure 13(a) shows the average of six blackbody calibration spectra for detector 1 with the 850 μm band (thick line) and the standard deviation in each resolution element (thin line). Figure 13(b) shows the corresponding average for detector 2. These graphs are typical of all the filter bands, and indicate that the noise is white both inside and outside the filter band pass. Using the S/N calculated from the maximum spectral intensity and the average noise in the band, we tabulate the NEPs calculated from Eq. (19) in Table II.

While these values are larger than those predicted in Sec. III, they represent the total FTS system noise when it is in operation on the noisy telescope Nasmyth platform.

V. DISCUSSION

In this article we have presented the design performance of a new dual polarizing detector system for use with a polarizing Fourier transform spectrometer to conduct broadband astronomical spectroscopy at submillimeter wavelengths. The design builds on experience gained with the recently retired, JCMT continuum receiver, UKT14. The cryogenic system is built around a closed cycle, dual stage,
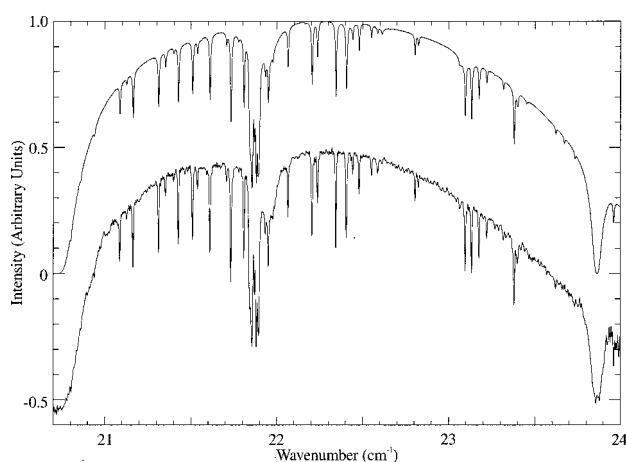
FIG. 14. Atmospheric transmission spectra from Mauna Kea in the 450 μm band: Single measured spectrum (lower trace) and theoretical model spectrum (upper trace).

^{4}He–^{3}He refrigerator which has proven to be both efficient and simple to operate. The optical design minimizes the background loading on the detectors and the amplitude of the ubiquitous channel fringes that are still evident in Fig. 13. A balanced differential electronics design has significantly improved the rejection of environmental noise. Detector NEP values determined from different approaches yielded consistent results (Table II). When account is taken of the optical efficiency, the equivalent NEP at the entrance window of the cryostat is $\sim 4 \times 10^{-15}$ W/$\sqrt{\text{Hz}}$. In conjunction with the polarizing FTS, under stable and dry observing conditions, this translates to a noise temperature of ~ 1 K in a bandwidth of 150 MHz at a wavelength of 850 μm with a 5 min integration.

An illustration of the spectral performance of the detector is given in Fig. 14, which shows a comparison between the atmospheric transmission in the 450 μm band, measured from Mauna Kea (lower trace) and the theoretical model (upper trace). The resulting spectrum is seen to be in excellent agreement with the model. This spectral region is dominated by absorption from atmospheric ozone. The measured spectra have symmetrical line shapes of 0.005 cm^{-1} full width at half maximum, and the uncertainty in the wavelength scale, as determined by comparison with the theoretical ozone line positions, is 0.0002 cm^{-1}. Analysis of the transmission spectra is ongoing, and the results will be presented elsewhere.

[1] T. G. Phillips, in *Millimeter and Submillimeter Astronomy*, edited by R. D. Wolstencroft and W. B. Burton (Kluwer Academic, Dordrecht, 1988), pp. 1–25.
[2] D. A. Naylor, G. R. Davis, M. J. Griffin, T. A. Clark, D. Gautier, and A. Marten, Astron. Astrophys. **291**, L51 (1994).
[3] E. Serabyn and E. W. Weisstein, Astrophys. J. **451**, 238 (1995).
[4] E. W. Weisstein and E. Serabyn, Icarus **123**, 23 (1996).
[5] D. A. Naylor and T. A. Clark, Proc. SPIE **627**, 482 (1986).
[6] D. A. Naylor, T. A. Clark, A. A. Schultz, and G. R. Davis, Mon. Not. R. Astron. Soc. **251**, 199 (1970).
[7] W. D. Duncan, E. I. Robson, P. A. R. Ade, M. J. Griffin, and G. Sandell, Mon. Not. R. Astron. Soc. **243**, 126 (1990).
[8] Chase Research, 35 Wolstenholm Road, Sheffield, S7 1LB, UK.
[9] Infrared Laboratories Inc., 1808 East 17th Street, Tucson, AZ 85719.
[10] D. A. Naylor, A. A. Schultz, and T. A. Clark, Appl. Opt. **27**, 2603 (1988).
[11] P. A. R. Ade, Proceedings of the Workshop on Bolometers for Submillimeter Space Projects, Orsay, France, IASRS95-02, June 1995.
[12] Goodfellow, Cambridge Science Park, Cambridge CB4 4BR, UK.
[13] D. A. Harper, R. H. Hildebrand, R. Steining, and R. Winston, Appl. Opt. **15**, 53 (1976).
[14] D. H. Martin, in *Infrared and Millimeter Waves*, edited by K. J. Button (Academic, New York, 1982), Vol. 6, pp. 65–148.
[15] E. E. Haller, Infrared Phys. **25**, 257 (1985).
[16] Chase Research, 35 Wolstenholm Road, Sheffield S7 1LB, UK.
[17] Lakeshore Cryotronics Inc., 64 East Walnut Street, Westerville, OH 43081-2399.
[18] H. P. Gush, M. Halpern, and S. Knotek, Rev. Sci. Instrum. **63**, 90 (1992).
[19] F. J. Low, Proc. SPIE **280**, 56 (1981).
[20] G. H. Rieke, E. F. Montgomery, M. J. Lebofsky, and P. R. Eisenhardt, Appl. Opt. **20**, 814 (1981).
[21] InterFET Corporation, 100 North Shiloh Road, Garland, TX 75042.
[22] Cochise Instruments Inc., 6304 deMello Street, Hereford, AZ 85615.
[23] W. S. Holland *et al.*, Mon. Not. R. Astron. Soc. **303**, 659 (1999).
[24] J. C. Mather, Appl. Opt. **21**, 1125 (1982).
[25] Research Systems Inc., 4990 Pearl East Circle, Boulder, CO 80301.
[26] M. J. Griffin and W. S. Holland, Int. J. Infrared Millim. Waves **9**, 861 (1988).
[27] R. R. Treffers, Appl. Opt. **16**, 3103 (1977).